Title

A promising single atom catalyst for CO oxidation: Ag on boron vacancies of h-BN sheets.

Journal

Physical chemistry chemical physics : PCCP, 19(25)

ISSN

1463-9076

Authors

Lu, Zhansheng
Lv, Peng
Yang, Zongxian
et al.

Publication Date

2017-06-01

DOI

10.1039/c7cp02430d

PCCP

PAPER

View Article Online
View Journal | View Issue

Cite this: *Phys. Chem. Chem. Phys.*, 2017, **19**, 16795

A promising single atom catalyst for CO oxidation: Ag on boron vacancies of h-BN sheets†

Zhansheng Lu,[ab] Peng Lv,[a] Zongxian Yang,*[ac] Shuo Li,[a] Dongwei Ma[d] and Ruqian Wu*[b]

Received 14th April 2017,
Accepted 1st June 2017

DOI: 10.1039/c7cp02430d

rsc.li/pccp

Single atom catalysts (SACs) have attracted broad research interest in recent years due to their importance in various fields, such as environmental protection and energy conversion. Here, we discuss the mechanisms of CO oxidation to CO_2 over single Ag atoms supported on hexagonal boron-nitride sheets (Ag_1/BN) through systematic van der Waals inclusive density functional theory (DFT-D) calculations. The Ag adatom can be anchored onto a boron defect (V_B), as suggested by the large energy barrier of 3.12 eV for Ag diffusion away from the V_B site. Three possible mechanisms (*i.e.*, Eley–Rideal, Langmuir–Hinshelwood, and termolecular Eley–Rideal) of CO oxidation over Ag_1/BN are investigated. Due to "CO-Promoted O_2 Activation", the termolecular Eley–Rideal (TER) mechanism is the most relevant one for CO oxidation over Ag_1/BN and the rate-limiting reaction barrier is only 0.33 eV. More importantly, the first principles molecular dynamics simulations confirm that CO oxidation *via* the TER mechanism may easily occur at room temperature. Analyses with the inclusion of temperature and entropy effects further indicate that the CO oxidation *via* the TER mechanism over Ag_1/BN is thermodynamically favorable in a broad range of temperatures.

1. Introduction

Carbon monoxide (CO) oxidation has attracted great interest due to its importance in various industrial and environmental applications,[1] and it has also become a benchmark reaction for examining the activity of heterogeneous catalysts.[2] Typical catalysts for CO oxidation consist of noble metals, such as Pt,[3–8] Pd,[5,6,9–12] Ru[13] and Au,[14–17] and they have been widely investigated for decades. To further increase the catalytic performance and reduce the cost, recent research attention has turned to "single atom catalysts" (SACs)[18,19] by downsizing the catalyst to the atomic scale, which provides a platform for the establishment of new fundamental science as well as the design of excellent catalysts.

Despite many major instrumental developments in surface science and nanoscience, the fabrication and characterization of stable SACs still remain very challenging because of the high mobility and the tendency of clustering of metal atoms on supporting materials.[20,21] Therefore, it is essential to find appropriate substrates that may strongly pin the metal species, yet maintain their high chemical activity. To this end, experimental research has shown that oxide supports such as MgO,[20] FeO_x,[19] SiO_2[22] and TiO_2[23] or graphitic layers[24] can anchor single metal atoms and hence allow synthesis of SACs by using the mass-selected soft-landing technique, improved wet chemistry methods, or atomic layer deposition methods.[19,20,24] Particularly, two-dimensional (2D) materials with a large surface area and high thermal stability, such as graphene,[25–29] graphyne,[30,31] MoS_2[32] and freestanding hexagonal boron nitride monolayers (h-BN),[33,34] can be used as prominent supports to host single metal atoms, which exhibit superb catalytic activity for CO oxidation.[35–38] Recent experimental studies also showed that Ag supported by BN nanosheets with good thermal stability can be used as an effective catalyst for the reduction of *p*-nitrophenol[39,40] and the methanol oxidation reaction.[41] Moreover, a SAC with Ag on MnO_x has been fabricated and proved to be efficient in catalyzing HCHO oxidation.[42,43] For the rational design of SACs and also for the optimization of their catalytic performance, it is very important to provide theoretical explanations of these experimental findings.

Here, we use a system with a single Ag atom supported on a hexagonal boron-nitride sheet (Ag_1/BN) as the prototype SAC and investigate its structural stability and catalytic activity

[a] *College of Physics and Materials Science, Henan Normal University, Xinxiang 453007, China. E-mail: yzx@henannu.edu.cn*
[b] *Department of Physics and Astronomy, University of California, Irvine, CA 92697-4575, USA. E-mail: wur@uci.edu*
[c] *Collaborative Innovation Center of Nano Functional Materials and Applications, Kaifeng, Henan Province, China*
[d] *School of Physics, Anyang Normal University, Anyang 455000, China*

† Electronic supplementary information (ESI) available: The various O_2 adsorption configurations over V_B/BN are presented in Fig. S1 and the first principles MD simulations of the CO oxidation *via* the TER mechanism can be seen in Movie S1. See DOI: 10.1039/c7cp02430d

toward CO oxidation through systematic *ab initio* calculations using the dispersion-corrected density functional theory (DFT-D). We aim to provide answers for the core questions regarding the design and use of SACs: (i) can single Ag atoms be dispersed and kept on h-BN? If so, (ii) can the Ag_1/BN configuration possess high catalytic activity toward the CO oxidation reaction? (iii) What is the most relevant mechanism for CO oxidation? The first principles molecular dynamics (MD) simulations and temperature/entropy analyses are also performed to appreciate the fundamental aspects and microscopic processes regarding the structural stability and reactivity of SACs, respectively. Our studies elucidate mechanisms of CO oxidation over Ag_1/BN and shed light on the principles for the design of more effective catalysts based on the SAC concept.

2. Computational details

All spin-unrestricted calculations are performed within the DFT-D framework as implemented in the DMol^3 code[44] which is embedded in Materials Studio (Accelrys, San Diego, CA). We employ the DFT semi-core pseudopotentials (DSPPs)[45] to describe the core–valence interactions. The generalized gradient approximation (GGA, in the form of the PBE functional)[46] with long-range dispersion correction *via* the Tkatchenko–Scheffler scheme is adopted throughout the calculations.[47] During the geometrical optimization, the real-space global cutoff radius is set to be 4.5 Å. The convergence tolerances for the geometry optimization are set to 10^{-5} Ha (1 Ha = 27.21 eV) for the energy, 0.002 Ha Å^{-1} for the force, and 0.005 Å for the displacement. The electronic self-consistent field (SCF) tolerance is set to 10^{-6} Ha. In order to achieve quick yet accurate electronic convergences, we apply a smearing of 0.005 Ha to the orbital occupation. The reciprocal space is sampled with a $(5 \times 5 \times 1)$ *k*-point grid generated automatically using the Monkhorst–Pack method[48] for the relaxation calculations. Within the schemes and parameters above, the B, N, C and O atoms are treated with all-electron basis-sets, while the core electrons of Ag are represented by a single effective pseudopotential including the relativistic effects, and the valence electrons of Ag are handled with the DNP basis-sets. The complete linear synchronous transit (LST)/quadratic synchronous transit (QST) method[49] at the same theoretical level is performed to locate the transition state (TS) in the DMol^3 approach. In this method, the LST maximization is performed, followed by an energy minimization in directions conjugated to the reaction pathway to obtain an approximated TS. The approximated TS is used to perform QST maximization and then another conjugated gradient minimization is performed. The cycle is repeated until a stationary point is located, which is an energy maximum in one direction (the direction of the reaction coordinate) and an energy minimum in all other directions. The geometric optimization and the search for transition states are tested by means of frequency calculations. Moreover, the first principles molecular dynamics (MD) simulations using the microcanonical *NVE* ensemble are performed to mimic the actual CO oxidation process over the Ag_1/BN surface.

The calculated lattice constant of h-BN is 2.51 Å and the corresponding B–N bond length is 1.45 Å, which are in good agreement with previous studies.[37] The BN support for the Ag_1–BN SAC is modeled by using a 4×4 h-BN supercell in the lateral plane, with a vacuum separation of 15 Å. Our test calculations suggest that the current model with the *k*-point grid is adequate for the investigation of CO oxidation. The adsorption energy (E_{ads}) is defined by:

$$E_{ads} = E_{adsorbate} + E_{support} - E_{adsorbate/support} \quad (1)$$

where $E_{adsorbate}$, $E_{support}$ and $E_{adsorbate/support}$ are the total energies of the free adsorbate, the bare support and the combined system, respectively. When co-adsorbates are involved, this equation can be extended for the determination of co-adsorption energy, *i.e.*, using the sum of energies of adsorbates in their gas phase in lieu of $E_{adsorbate}$. All energies need to be derived from calculations using the same unit cell and the same computational setting. With this definition, a positive E_{ads} indicates an exothermic adsorption. It is noticeable that the basis set superposition error (BSSE) correction is not considered in the current study. It has been confirmed that the BSSE in the DNP basis set in DMol^3 is much smaller than that in the similar sized Gaussian basis set, *i.e.*, the numerical basis sets implemented in DMol^3 can minimize or even eliminate the BSSE.[50,51]

The charge density difference (CDD, $\Delta\rho$) can be used to appreciate the interaction between the support and the adsorbate. It is defined as:

$$\Delta\rho = \rho_{adsorbate/support} - \rho_{adsorbate} - \rho_{support} \quad (2)$$

where $\rho_{adsorbate/support}$, $\rho_{adsorbate}$, and $\rho_{support}$ are the corresponding charge densities of the combined system, the free adsorbate, and the bare support, respectively. In the figures, the values of isosurfaces of CDD are fixed at $\pm$0.02 a.u., with green and red colors denoting the charge accumulation and charge depletion, respectively.

3. Results and discussion

3.1 Structural stability of single Ag adatoms over h-BN

To study the catalytic activity of Ag_1/BN towards CO oxidation, the structural stability of an Ag adatom over h-BN should be examined first. To this end, the adsorption geometries of the Ag atom over four typical sites on the pristine h-BN layer are considered: the hollow site of the hexagon (T_H), the top sites over boron (T_B) and nitrogen (T_N), as well as the bridge site between boron and nitrogen (T_{bri}). The T_H, T_B and T_N sites are found to be stable or metastable for the Ag adatom to occupy, as shown in Fig. 1a–c. The corresponding distances between Ag and its nearest B (or N) atoms are 3.67, 3.14, and 3.41 Å, respectively. The structural distortion and charge rearrangement in h-BN are negligible, suggesting a weak interaction between the single Ag atom and the perfect h-BN sheet. Accordingly, the calculated adsorption energies of single atomic Ag on the three sites mentioned above are 0.33, 0.36 and 0.33 eV, respectively, all of which are much smaller than the calculated binding energy of

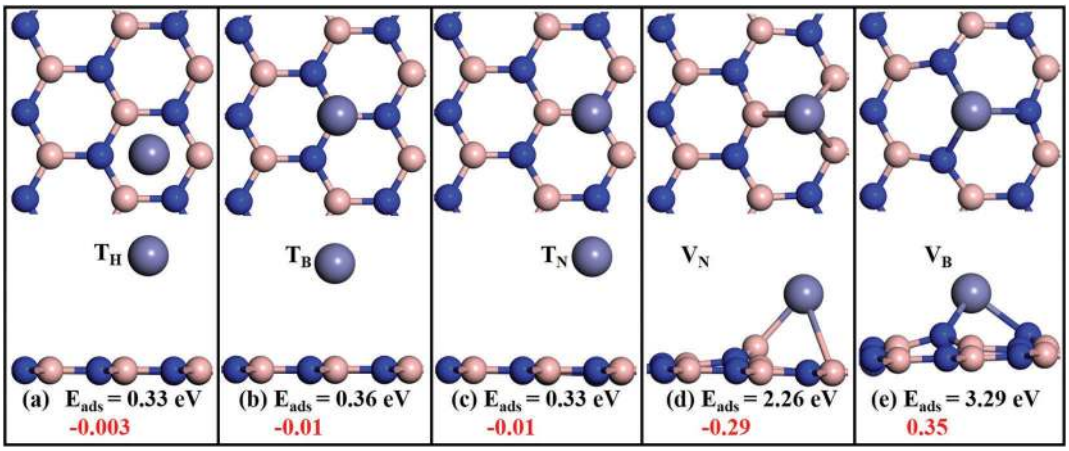

Fig. 1 Top and side views of the most stable configurations of single atomic Ag adsorbed on a (a) hollow site, (b) top site of the boron atom, (c) top site of the nitride atom, (d) nitride vacancy and (e) boron vacancy of the support, respectively. The corresponding adsorption energies and Mulliken charges (|e|) are inserted in the picture in black and red, respectively. Hereafter, the pink, blue and purple spheres represent B, N and Ag, respectively.

Ag in an Ag_2 dimer (0.84 eV) or in the bulk fcc Ag (2.95 eV). Obviously, the pristine h-BN layer cannot anchor Ag adatoms well and it is perceivable that Ag atoms tend to form clusters.

As widely reported, surface vacancies of supporting materials may serve as excellent anchoring sites to trap single atoms.[29,52–54] Interestingly, the nitrogen (V_N) and boron (V_B) vacancies of h-BN with dangling bonds have been successfully fabricated by using irradiation with high energy electrons in experiments,[55] and the defective h-BN was believed to serve as a good support for SACs for CO oxidation, with adatoms like Co, Pd, Pt, Au, and Fe.[33,35–37,56] Here, we explore various possibilities of having a single Ag adatom on the defective h-BN, and the most stable configurations are presented in Fig. 1d and e (defined as Ag_1–V_N/BN and Ag_1–V_B/BN). The Ag adatom on either V_N or V_B stays out of the BN plane because of its relatively large atomic radius, and the adjacent atoms in BN are also lifted upwards. The Mulliken charge analysis shows that the single Ag atom over V_N is negatively charged by 0.29 $|e|$, and different electron donation amounts are found for the three B atoms around the atomic Ag (0.14, 0.02, 0.02 electrons, respectively), indicating that the three neighboring B atoms are non-equivalent. Thus, Ag prefers to bind more tightly with one B atom to have a stronger ionic interaction and the length of the three Ag–B bonds in Ag_1–V_N/BN are different: 2.17, 2.73 and 2.73 Å, respectively. In contrast, states around V_B are more delocalized and Ag donates the same electrons to its three neighboring N atoms in Ag_1–V_B/BN. Thus, the three neighboring N atoms are equivalent and the three Ag–N bonds are equal in length: 2.10 Å, which is consistent with the previous result of 2.12 Å.[33] The corresponding adsorption energies of Ag on the V_N/BN and V_B/BN configurations are 2.26 and 3.29 eV, respectively. Note that the adsorption energy of Ag over V_B/BN is even larger than the binding energy in the bulk Ag (2.95 eV); it is reasonable to assume that Ag disperses on V_B sites rather than clustering if the coverage is controlled below the density of defects in the BN layer. Moreover, the diffusion barrier for the Ag adatom to drift away from one V_B site to another stable adsorption site near the B vacancy is as high as 3.12 eV, as shown in Fig. 2a, which is noticeably larger than that for Cu on defective graphene of 2.34 eV.[57] According to the conventional transition state theory,

$$\tau \propto \nu^{-1} \exp(-E/kT) \quad (3)$$

one may estimate that the time duration (τ) for Ag staying on a V_B site is extremely long (>1000 days at 750 K, with a prefactor of $\nu = 10^{13}$ 1 s^{-1}). Therefore, the Ag_1–V_B/BN configuration is extraordinarily stable even at a reasonably elevated temperature for typical chemical reactions.

To understand the physical properties of Ag_1–V_B/BN, the plots of partial density of states (PDOS) are presented in Fig. 2b. From the symmetric PDOS curves for the two spin channels, the spin magnetism of this system is zero. There are four peaks that stem from Ag-4d states and N-2p states near the Fermi level (E_F), indicating the significant orbital hybridization between Ag and its neighboring N. Moreover, the large charge transfer from Ag to the support is also confirmed by the Mulliken charge analysis (0.35 $|e|$) and the CDD (inset of Fig. 2b). The CDD shows that the charge rearrangement mainly occurs around the three neighboring N atoms of Ag. Obviously, both orbital hybridization and charge transfer are indicative of a strong interaction between Ag and h-BN with a boron vacancy.

3.2 Adsorption of species involved in the CO oxidation over Ag_1–V_B/BN

To study the CO oxidation reaction over Ag_1–V_B/BN, the adsorption and co-adsorption of reactants, *i.e.*, CO and O_2, are investigated. The most stable adsorption configurations and their corresponding adsorption energies are summarized in Fig. 3, along with the corresponding CDD maps and geometrical parameters. It is found that all species prefer to stay over the Ag atom with reasonably high values of E_{ads}.

The most stable configuration of O_2 adsorption is with the two oxygen atoms symmetrically binding to the Ag atom (side-on model) with short Ag–O bonds (2.17 Å), and is similar to those of O_2 on Co and Fe-doped h-BN,[33] but different from the end-on

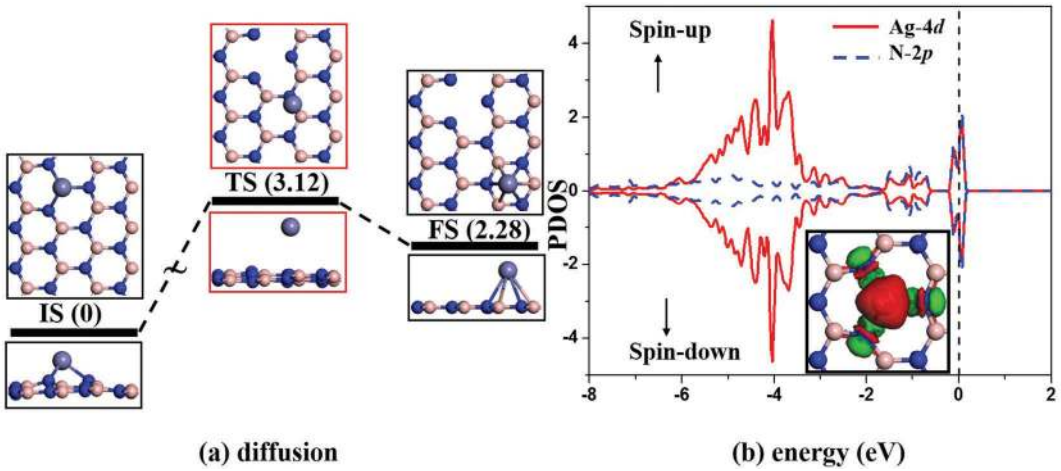

Fig. 2 (a) The reaction profile for the diffusion of a single Ag atom from its most stable adsorption site to another stable adsorption site near the B vacancy. The corresponding E_{ads} for Ag on this site is 1.01 eV. All energy values are in eV. (b) The spin-polarized partial density of states (PDOS) projected on Ag-4d (red) and N-2p (blue) states. The Fermi level is set to zero. The CDD for the single Ag atom over V_B/BN is also presented as an inset.

adsorption model for O_2 on Si-doped h-BN[58] and BN nanotubes.[59] The calculated E_{ads} of O_2 is moderate, 0.86 eV. According to the Mulliken charge analysis, O_2 is negatively charged by 0.30 $|e|$ over Ag_1–V_B/BN, and the Ag adatom is positively charged by 0.52 $|e|$. Therefore, O_2 acts as the electron acceptor while Ag_1–V_B/BN acts as the electron donor. The consequence of the sizeable charge transfer from Ag to O_2 is the occupation of the $2\pi^*$ orbitals of O_2, which leads to a significant elongation of the O–O bond (from 1.23 Å to 1.31 Å). This is also confirmed by the CDD (presented in Fig. 3a): the charge depletion region (red) is mainly around the Ag atom and the charge accumulation region (green) shows a feature of donuts around the two O atoms. Furthermore, the $2\pi^*$ orbitals of the O_2 molecule over Ag_1–V_B/BN are partially occupied (see the PDOS presented in Fig. 4a). The elongation of the O–O bond and the large charge transfer from Ag to O_2 suggest the activation of the O_2 molecule by the single Ag atom,[60] which is necessary for the CO oxidation. We also investigate the thermal stability of single atomic Ag over V_B/BN in the presence of O_2. It is found that the E_{ads} of the most stable O_2 adsorption over V_B/BN is 1.70 eV (see Fig. S1a in the ESI†). This value is much smaller than that for Ag (3.29 eV), and hence the O_2 molecule is very unlikely to swap with Ag over V_B/BN. This is important since it indicates that the SAC of Ag_1–V_B/BN is thermally stable against oxygen adsorption.

Fig. 3b presents the most stable configuration of CO adsorption over Ag_1–V_B/BN, which takes the end-on configuration with the formation of a Ag–C (2.03 Å) bond. The calculated E_{ads} of CO is 1.04 eV, in agreement with the previous result (1.07 eV) reported by Lin *et al.*[33] This value is 0.18 eV higher than that for the O_2 adsorption, suggesting that Ag_1–V_B/BN is more attractive toward CO. Upon CO adsorption, CO-$2\pi^*$ orbitals are also partially occupied because some electrons transfer from Ag to the CO-$2\pi^*$ orbitals (Fig. 4b). The Mulliken charge analysis shows

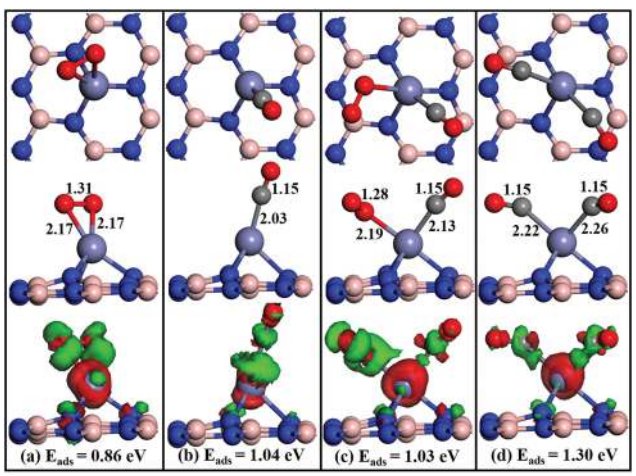

Fig. 3 Top and side views as well as the CDD maps of the most stable adsorption configurations of (a) O_2, (b) CO, (c) CO + O_2, and (d) CO + CO adsorbed over Ag_1–V_B/BN. The adsorption/co-adsorption energies and the selected geometric parameters are also presented in the pictures. Hereafter, the red and gray spheres represent O atoms and C atoms, respectively.

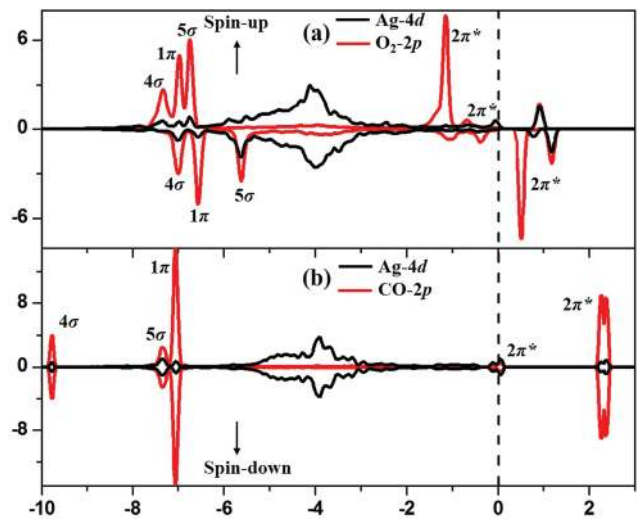

Fig. 4 PDOS for (a) O_2 and (b) CO adsorption over Ag_1–V_B/BN. The Fermi level is set to zero.

that CO is positively charged by 0.11 $|e|$, which is the result of the donation of CO-5σ electrons to Ag-4d states and the back-donation of Ag-4d electrons into the CO-2π* orbitals.[32,61] Moreover, a previous study has shown that the HOMO of the CO molecule (5σ) has weight mainly around the C atom,[62] indicating that CO always acts as a donor when its C end points to the anchoring atom. The current phenomenon is similar to the positively charged CO over Al/graphene,[28] Pd/BN[56] and Pt/BNNT.[63] Both the 5σ and 1π orbitals of CO hybridize with the Ag-4d states in the energy range from −8 eV to −6 eV, and the two Ag-4d peaks near the Fermi level also overlap with the 2π* orbitals of CO, confirming the strong interaction between Ag and CO.

In order to investigate the reaction mechanism by which CO oxidation proceeds on the surface, it is also necessary to study the capture performance (co-adsorption of the reactants) over Ag_1–V_B/BN. According to the adsorption energies discussed above, CO more favourably takes the Ag site when the two reactant gases (CO and O_2) are injected simultaneously. When CO is pre-adsorbed, the forthcoming O_2 or CO molecules form co-adsorption configurations on CO/Ag_1–V_B/BN, either CO + O_2 (Fig. 3c) or CO + CO (Fig. 3d), and their co-adsorption energies are 1.03 and 1.30 eV. Note that the co-adsorption energy of CO + O_2/Ag_1–V_B/BN is slightly smaller than that of CO/Ag_1–V_B/BN but larger than that of O_2/Ag_1–V_B/BN. One may perceive that CO and O_2 are somewhat repulsive over Ag_1–V_B/BN and it is unlikely to have an O_2 molecule landing on CO/Ag_1–V_B/BN. On the other hand, as discussed below, it is also hard to add CO on O_2/Ag_1–V_B/BN, so the co-adsorption of CO + O_2/Ag_1–V_B/BN is a rare case. In contrast, the co-adsorption of CO + CO (Fig. 3d) is more favorable than the adsorption of a single CO, with the V-shape O–C–Ag–C–O structure. This shows that each Ag adatom over V_B/BN can host two CO molecules. The CDD in Fig. 3d shows the charge transfer between Ag and CO (each CO is positively charged by 0.08 $|e|$).

3.3 CO oxidation over Ag_1–V_B/BN

In general, CO oxidation on catalysts may occur *via* either the Eley–Rideal (ER) mechanism or the Langmuir–Hinshelwood (LH) mechanism.[4,64] In the ER mechanism, the gas-phase CO molecule directly reacts with the pre-adsorbed and activated O_2 to form a carbonate-like intermediate (CO_3) or the final product of CO_2. The LH mechanism involves the co-adsorption of O_2 and CO molecules, the formation and dissociation of a peroxide-like (OCOO) complex intermediate, and finally desorption of CO_2. It was found that the ER mechanism is the dominant pathway for CO oxidation on some catalysts, such as the Fe-anchored graphene oxide, SiC monolayers and N-doped carbon nanotubes.[65–67]

Here, both ER and LH mechanisms are systematically investigated through DFT-D calculations. As mentioned above, O_2 is readily activated over Ag_1–V_B/BN, and hence CO oxidation is likely *via* the ER mechanism. As shown in Fig. 5, the configuration of physisorbed CO above O_2/Ag_1–V_B/BN is used as the initial state (IS). In the first step of reaction, CO binds to O_2 to form the CO_3 species with a high reaction barrier of 1.80 eV. Although the entire reaction to the final state (FS, CO_2 + O/Ag_1–V_B/BN) is exothermic, with a reaction energy of 2.20 eV, the ER mechanism for the CO oxidation is essentially prohibited in the first step.

The initial state of the LH mechanism is the co-adsorption of CO and O_2 over Ag_1–V_B/BN. As discussed in the previous section, this is a rare configuration and hence the LH mechanism is not applicable for CO oxidation over Ag_1–V_B/BN. Nevertheless, as shown in Fig. 6, the reaction barriers for sequential steps are less than 0.53 eV and the entire reaction process is exothermic with a reaction energy of 1.89 eV. Therefore, CO may oxidize through the LH mechanism if the gas pressure is high or the residue time of the CO + O_2/Ag_1–V_B/BN configuration is sufficiently long. Since this configuration may form dynamically with either CO hitting from the side of O_2/Ag_1–V_B/BN (instead from the top of O_2 as

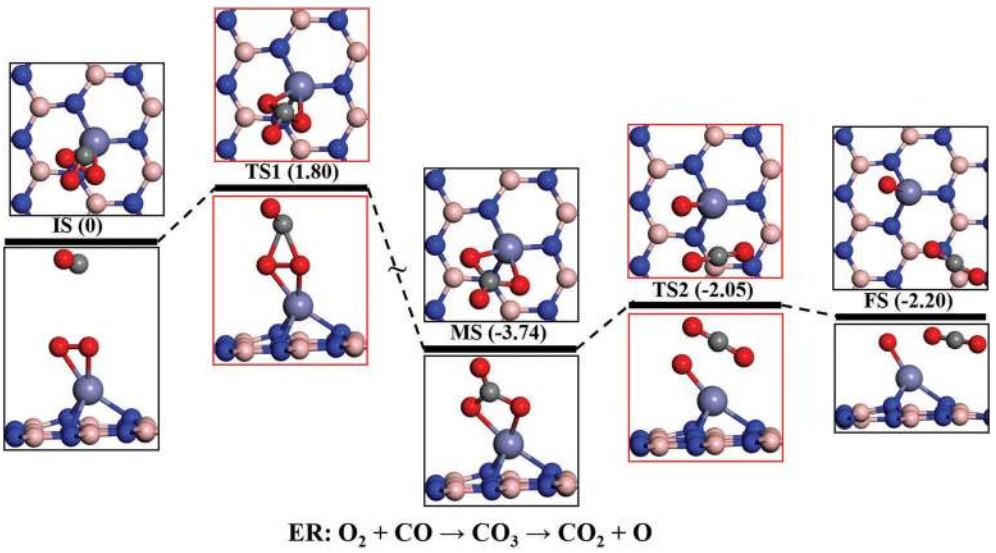

Fig. 5 The reaction profile of CO oxidation *via* the ER mechanism. Hereafter, the local configurations of the adsorbates over Ag_1–V_B/BN at initial states (IS), transition states (TS), intermediate states (MS) and final states (FS) along the minimum-energy pathway are shown in the insets, respectively. All energies are given with respect to the reference energy (eV).

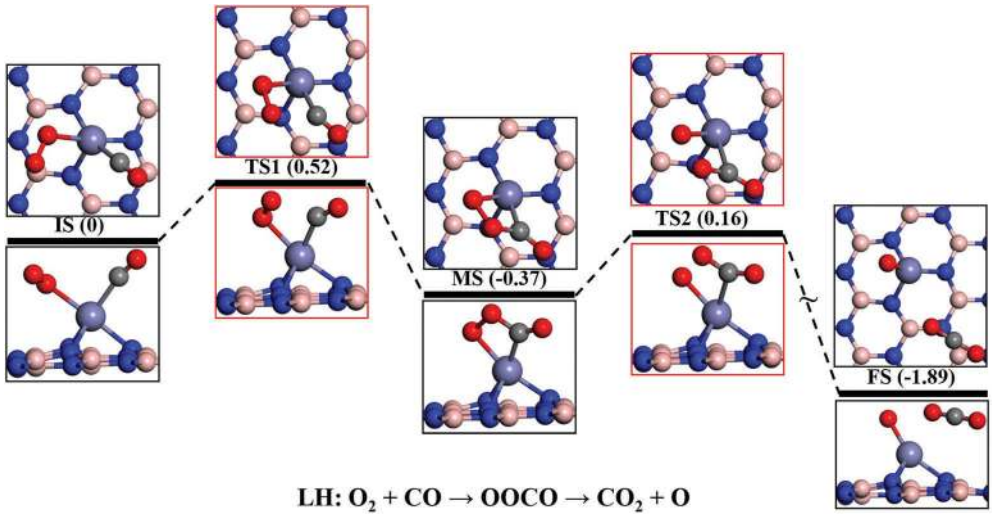

Fig. 6 The reaction profiles of CO oxidation *via* the LH mechanism. All energies are given with respect to the reference energy (eV).

depicted in Fig. 5) or O_2 hitting from the side of $CO/Ag_1–V_B/BN$, it is hard to distinguish the ER and LH mechanisms.

The LH mechanisms produce a CO_2 molecule and an $O/Ag_1–V_B/BN$ configuration, where the CO_2 molecule is physisorbed with a rather small adsorption energy, 0.26 eV, and hence it should be easily released under ambient conditions. The atomic O species is believed to be more reactive than O_2,[68,69] and the atomic O left over the $Ag_1–V_B/BN$ catalyst can also be easily removed *via* the reaction process: $O + CO \rightarrow CO_2$. As shown in Fig. 7, the configuration of physisorbed (2nd) CO above $O/Ag_1–V_B/BN$ is set as IS for the reaction. The reaction barrier for the formation of the second CO_2 molecule is only 0.17 eV and the reaction releases a large heat of 4.01 eV. Therefore, the recovery of the $Ag_1–V_B/BN$ SAC for the next round of reaction should not be an issue for the LH mechanism, provided it can occur under the conditions mentioned above.

Obviously, the CO oxidation may also start from the CO + $CO/Ag_1–V_B/BN$ co-adsorption configuration as depicted in Fig. 3d. Fig. 8 presents the reaction profile of the termolecular Eley–Rideal mechanism (TER),[36] in which a free O_2 molecule can be activated by the two co-adsorbed CO molecules to form an OCO–metal–OCO intermediate (CO-Promoted O_2 Activation). Here, in the initial state, two CO molecules are chemically co-adsorbed on the Ag site and one O_2 molecule approaches them from top, which is different from the termolecular LH mechanism.[70] Once a free O_2 is close enough, two oxygen atoms bind to the carbon atoms and form an OCO–Ag–OCO intermediate (MS), with a rather small reaction barrier of 0.10 eV and a sizable exothermic reaction energy of 1.25 eV. The OCO–Ag–OCO intermediate has a pentagonal ring structure (see the MS in Fig. 8), in which the O–O bond expands to 1.48 Å. Following the cleavage of the O–O bond, the OCO–Ag–OCO intermediate dissociates to two CO_2 molecules (see the FS in Fig. 8) with a reaction barrier of 0.33 eV and a huge exothermic reaction energy of 4.63 eV. Since the adsorption energy of CO_2 is only 0.36 eV, they should be desorbed spontaneously from $Ag_1–V_B/BN$ and finish the reaction cycle.

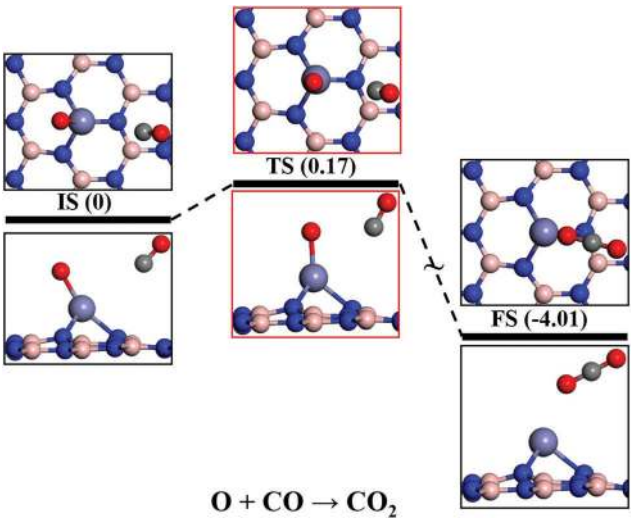

Fig. 7 The reaction profile of CO oxidation by the atomic O. All energies are given with respect to the reference energy (eV).

To highlight the excellent activity of the $Ag_1–V_B/BN$ catalyst for CO oxidation, a comparison of reaction barriers of the rate-limiting step with several other systems is summarized in Table 1. Obviously, the reaction barrier of the rate-limiting step *via* the TER mechanism for CO oxidation over $Ag_1–V_B/BN$ (0.33 eV) is lower than those on all noble metal catalysts (0.53–1.01 eV). Moreover, $Ag_1–V_B/BN$ is comparable to other graphene and h-BN based SACs but with better structural stability, as seen from the high energy costs for removing and shifting the Ag atom from the V_B site. Thus, it is worthwhile for experimental groups to examine the fabricability, endurability and catalytic performance of $Ag_1–V_B/BN$ for CO oxidation.

The electronic structure analysis in the PDOS and molecular orbitals may lead to a deeper understanding of the "CO-Promoted O_2 Activation". As shown in Fig. 9a, the hybridization between the CO-2p and Ag-4d states in the energy range of −8 to −6 eV and around the Fermi level is responsible for the interaction between

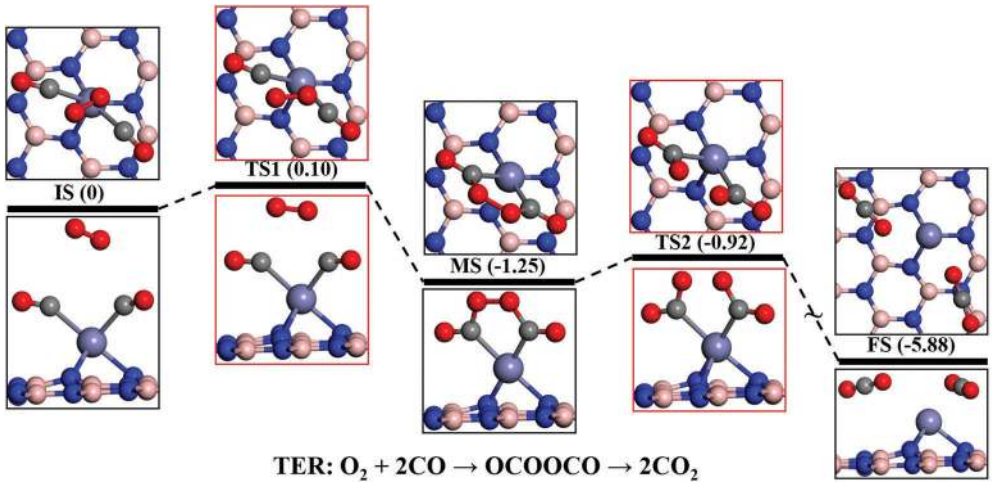

Fig. 8 The reaction profile of CO oxidation *via* the TER mechanism. All energies are given with respect to the reference energy (eV).

Table 1 Reaction barriers of the rate-limiting step for CO oxidation over several other nano-catalysts *via* the corresponding mechanisms

Catalyst	Barrier^{mechanism} (eV)	Catalyst	Barrier^{mechanism} (eV)
Ag_{55} cluster[71]	0.53^{ER}, 0.75^{LH}	Au_{55} cluster[61]	0.79^{LH}
Pt(111)[3]	1.01^{LH}	Au(221)[16]	0.59^{LH}
Fe_1/graphene[29]	0.58^{ER}	Cu_1/graphene[57]	0.54^{LH}
Au_1/graphene[72]	0.31^{LH}	Pt_1/graphene[73]	0.77^{ER}, 0.59^{LH}
Sn_1/graphene[74]	0.41^{LH}	SiN_4/graphene[75]	1.08^{ER}, 0.72^{LH}
Co_1/BN[33]	0.52^{ER}	Pt_1/BN[35]	1.31^{ER}, 0.38^{LH}
Au_1/BN[36]	0.72^{LH}, 0.47^{TER}	Fe_1/BN[37]	0.61^{ER}
Pd_1/BN[56]	1.29^{ER}, 0.66^{LH}, 0.39^{TER}	Ru_1/BN[76]	0.42^{ER}, 0.77^{LH}
C_1/BN[77]	0.26^{ER}	O_1/BN[77]	0.16^{ER}, 1.55^{LH}
Ag_1/BN	0.33^{TER} (current result)		

Ag and two CO molecules. From the Mulliken charge analysis, the two CO molecules are positively charged by 0.08 $|e|$ per molecule and the carbon atom is positively charged by 0.16 $|e|$, indicating that the adsorbed CO may act as electron donors for the electrophilic O_2 and facilitate the O_2 activation. The PDOS of TER-IS and TER-MS presented in Fig. 9b and c further reveals the mechanisms of ''CO-Promoted O_2 Activation''. One may find the partial occupation of the $2\pi^*$ orbitals of CO and O_2 near the E_F in Fig. 9b for the O_2/2CO/Ag_1–V_B/BN geometry. This suggests that the O_2 is already somehow activated by the two pre-adsorbed CO molecules and thus the energy cost to break the O–O bond becomes low. Indeed, the overlap between O_2-2p states and two CO-2p states is found in the entire energy range (Fig. 9c), which confirms the strong interaction between O_2 and CO in TER-MS and the ''CO-Promoted O_2 Activation''. From the isosurfaces of frontier molecular orbitals in Fig. 9d, we may find that the lowest unoccupied molecular orbital (LUMO) of the O_2 molecule matches well with the highest occupied molecular orbital (HOMO) of 2CO/Ag_1–V_B/BN. This explains why CO may hybridize with the LUMO ($2\pi^*$ orbitals) of O_2 and transfer electrons to it and lead to the O–O bond breaking.[78]

The CO oxidation process *via* the TER mechanism we proposed above can be better appreciated through the first principles molecular dynamics (MD) simulation (see Fig. 10 and Movie S1 in the ESI†). Some snapshots of the intermediate configurations are inserted in the figure. The two chemisorbed CO molecules with one physisorbed O_2 molecule are taken as the initial structure. It is found that one of the oxygen atoms in O_2 binds to the adjacent carbon atom at about 112 fs. At about 264 fs, both oxygen atoms in O_2 bind to their neighboring carbon atoms and the OCO–Ag–OCO intermediate forms. At about 480 fs, the O–O bond is broken and this step lasts for a long time: about 200 fs. Finally, two physisorbed CO_2 molecules are observed at 666 fs. Note that the dissociation of the OCO–Ag–OCO intermediate needs more time than its formation, which is in agreement with the larger reaction barrier of OCO–Ag–OCO dissociation (0.33 eV) than that for its formation (0.10 eV). In the following, the two CO_2 molecules depart from Ag_1–V_B/BN and the catalyst is refreshed. Actually, the first principles MD simulations for the CO oxidation process *via* the ER and LH mechanisms have also been performed. We found that no CO_3 species forms in 2 ps at 300 or 400 K, which is in accordance with the high reaction barrier of 1.80 eV for the formation of CO_3 through the ER mechanism. Our first principles MD simulations for the LH mechanism also show that the formation of OOCO species from co-adsorbed CO and O_2 over Ag_1–V_B/BN is also absent within 2 ps at 300 and 400 K and O_2 even starts desorbing from the Ag site at 400 K. Obviously, these results agree with the analysis that the co-adsorption of CO and O_2 is less preferable than co-adsorption of two CO (Fig. 3). The LH mechanism may take place only when the concentration of O_2 is much higher than that of CO in their mixed feed.

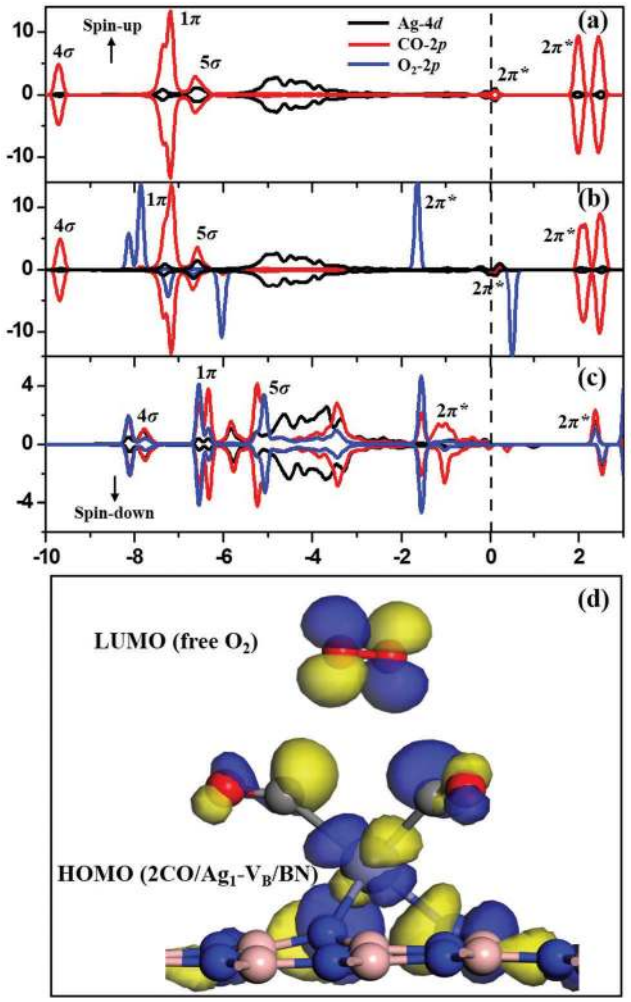

Fig. 9 PDOS for (a) two CO molecules in their co-adsorption configuration and (b) TER-IS and (c) TER-MS. The Fermi level is set to zero. (d) The LUMO of a free O_2 molecule and the HOMO of Ag_1–V_B/BN with pre-adsorption of two CO molecules.

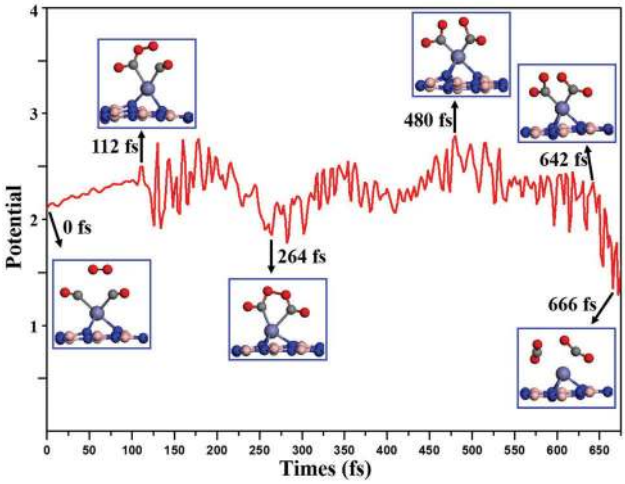

Fig. 10 The first principles MD simulations of CO oxidation *via* the TER mechanism: a time step of 2 fs is used and the temperature of the system is controlled at 300 K (room temperature). Here, only the trajectory from 0 fs to 675 fs (physisorbed CO_2 molecules are observed at 666 fs) is presented with some snapshots shown as the insets for some typical points for some important transitions.

Sabatier's principle[79,80] states that adsorbate–catalyst interactions should not be too weak or too strong to occur for a reaction, indicating that a moderate interaction between the active sites and adsorbate is important for the catalytic activity. In the current work, we also calculate the Sabatier activity for the three mechanisms based on previous work.[77] It is noticeable that the higher the Sabatier activity, the more favorable the mechanism. It is found that the Sabatier activity for the TER mechanism is 1.16 eV at room temperature, which is higher than those for the LH (1.00 eV) and ER (−0.39 eV) mechanisms. The Sabatier activity calculation also confirms that the TER mechanism is the most relevant one for CO oxidation over Ag_1–V_B/BN and this SAC is an effective catalyst.

3.4 Contribution of van der Waals correction

The long-range van der Waals (vdW) interaction in the Tkatchenko–Scheffler scheme[47] (DFT-D) is used to simulate the CO oxidation over Ag_1–V_B/BN. It would be necessary to check the energetics of CO oxidation, with and without vdW correction. We have tested the CO oxidation over Ag_1–V_B/BN through the TER mechanism, and found that all energies are changed very slightly between the DFT and DFT-D methods. For example, compared to the DFT method, the adsorption energies of O_2 in IS and MS, and CO_2 molecules in FS are slightly increased by 0.05, 0.07 eV and 0.19 eV because of the vdW correction, respectively. And the reaction barriers for the formation (TS1) and dissociation (TS2) of MS are decreased by 0.05 eV and 0.06 eV because of the vdW correction, respectively. Correspondingly, the reaction energies for those two steps also have a negligible change (slightly increased by 0.02 and 0.04 eV, respectively). Obviously, the use of vdW correction won't affect the results. Our stringent tests for benzene on Ag(110) showed that the DFT-D gives very reasonable results for binding energies and vibration frequencies.[81]

3.5 Effect of temperature and entropy

In order to provide a more realistic picture of the catalytic reaction, the temperature (T) and entropy (S) effects to assess the reaction thermodynamics of the induced CO oxidation over Ag_1–V_B/BN need to be considered explicitly.

The reaction thermodynamics for the CO oxidation *via* the ER and LH mechanisms have been successfully investigated over Fe coordinated N-doped carbon and Cr doped phthalocyanine catalysts.[82,83] However, very few reports involve the temperature and entropy dependence of the "TER" mechanism for CO oxidation. Here, the corrected free energy change for CO oxidation according to the temperature and entropy[84,85] is investigated, as shown in Table 2. The change in free energy is defined by the following formula:

$$\Delta G = \Delta E + \Delta E_{ZPE} - T\Delta S \quad (4)$$

where ΔG denotes the change in the Gibbs free energy between two successive steps of the TER mechanism. ΔE is the change in total energy at 0 K, and ΔE_{ZPE} is the change in zero point vibration

Table 2 Corrected free energy change (ΔG, eV) and $T\Delta S$ (eV) for each step in the CO oxidation reaction *via* the TER mechanism under various temperatures

	IS → MS ($2CO + O_2 \rightarrow OCO–Ag–OCO$)		MS → FS ($OCO–Ag–OCO \rightarrow 2CO_2$)		IS → FS ($2CO + O_2 \rightarrow 2CO_2$)	
T (K)	$T\Delta S$	ΔG	$T\Delta S$	ΔG	$T\Delta S$	ΔG
No correction	—	−1.25	—	−4.63	—	−5.88
250	−0.17	−0.90	0.17	−4.76	0	−5.66
298.15	−0.21	−0.86	0.20	−4.79	−0.01	−5.65
350	−0.25	−0.82	0.24	−4.83	−0.01	−5.65
400	−0.28	−0.79	0.27	−4.86	−0.01	−5.65
450	−0.31	−0.76	0.31	−4.90	0	−5.66
500	−0.34	−0.73	0.34	−4.93	0	−5.66

energy. ΔS is the change in entropy and ΔS is defined as $\Delta S_{vib} + \Delta S_{rot} + \Delta S_{trans}$, where ΔS_{vib}, ΔS_{rot} and ΔS_{trans} are the contributions of vibration, rotation and translation modes, respectively.

The T-dependent $T\Delta S$ is one of the most important factors determining the catalytic reaction. From Table 2, it is found that the two different reaction steps of the TER mechanism present distinct behaviors with the increase of T. The decrease of $T\Delta S$ causes the increase of ΔG as T varies from 250 to 500 K for the OCO–Ag–OCO formation, while that for the OCO–Ag–OCO dissociation step decreases with T. It is noticeable that the ΔG values of the whole reaction for different temperatures are negative, which indicates the thermodynamic favorableness of the CO oxidation *via* the TER mechanism over the Ag_1–V_B/BN catalyst at lower and higher temperatures.

4. Conclusion

The electronic structure and the mechanisms of CO oxidation to CO_2 over the SAC, Ag_1/BN, are systematically studied by DFT-D calculations. The calculated results show that:

(i) Ag atoms can be anchored on defective h-BN with a boron vacancy, according to the adsorption energy and diffusion barrier for a single Ag atom over V_B/BN.

(ii) According to the calculated reaction barriers of the rate-limiting steps of different CO oxidation mechanisms (ER, LH, TER), it is concluded that both the traditional LH (0.53 eV) and TER mechanisms (0.33 eV) for CO oxidation are possible at a low temperature.

(iii) Because of ''CO-Promoted O_2 activation'', the TER mechanism is the most relevant one for CO oxidation over Ag_1–V_B/BN. More importantly, the first principles MD simulations confirm that the CO oxidation *via* the TER mechanism may occur at room temperature. Analyses with the inclusion of temperature and entropy effects further indicate that the CO oxidation *via* the TER mechanism over Ag_1–V_B/BN catalyst is thermodynamically favorable in a broad range of temperatures.

Our studies elucidate mechanisms of CO oxidation over Ag_1/BN and shed light on the principles for the design of more effective catalysts based on the SAC concept.

Acknowledgements

Work at UCI was supported by the National Science Foundation Center for Chemical Innovation on Chemistry at the Space-Time Limit (CaSTL) under Grant No. CHE-1414466. Work at HNU was supported by the National Natural Science Foundation of China (Grant No. 51401078, 11474086 and U1504108); the Program for Science & Technology Innovation Talents in Universities of Henan Province (Grant No. 15HASTIT016); the Foundation for the key Young Teachers of Henan Province and Key Technology Research and Development Program of Henan Province (Grant No. 152102210083 and 142102210455); and the Science Foundation for the Excellent Youth Scholars of Henan Normal University (Grant No. 14YQ005). This work was also supported by the High Performance Computing Center of Henan Normal University.

References

1 J. Xu, Y.-Q. Deng, Y. Luo, W. Mao, X.-J. Yang and Y.-F. Han, *J. Catal.*, 2013, **300**, 225–234.
2 H. J. Freund, G. Meijer, M. Scheffler, R. Schlögl and M. Wolf, *Angew. Chem., Int. Ed.*, 2011, **50**, 10064–10094.
3 A. Alavi, P. Hu, T. Deutsch, P. L. Silvestrelli and J. Hutter, *Phys. Rev. Lett.*, 1998, **80**, 3650–3653.
4 K. Bleakley and P. Hu, *J. Am. Chem. Soc.*, 1999, **121**, 7644–7652.
5 A. Eichler, *Surf. Sci.*, 2002, **498**, 314–320.
6 X.-Q. Gong, Z.-P. Liu, R. Raval and P. Hu, *J. Am. Chem. Soc.*, 2004, **126**, 8–9.
7 I. Nakai, H. Kondoh, K. Amemiya, M. Nagasaka, A. Nambu, T. Shimada and T. Ohta, *J. Chem. Phys.*, 2004, **121**, 5035–5038.
8 I. Nakai, H. Kondoh, K. Amemiya, M. Nagasaka, T. Shimada, R. Yokota, A. Nambu and T. Ohta, *J. Chem. Phys.*, 2005, **122**, 134709.
9 D. Palagin and J. P. K. Doye, *Phys. Chem. Chem. Phys.*, 2015, **17**, 28010.
10 P. Salo, K. Honkala, M. Alatalo and K. Laasonen, *Surf. Sci.*, 2002, **516**, 247–253.
11 S. Shan, V. Petkov, L. Yang, J. Luo, P. Joseph, D. Mayzel, B. Prasai, L. Wang, M. Engelhard and C.-J. Zhong, *J. Am. Chem. Soc.*, 2014, **136**, 7140–7151.
12 Y. Zhou, Z. Wang and C. Liu, *Catal. Sci. Technol.*, 2015, **5**, 69–81.
13 C. Stampfl and M. Scheffler, *Phys. Rev. Lett.*, 1997, **78**, 1500–1503.
14 M. L. Kimble, A. W. Castleman, R. Mitrić, C. Bürgel and V. Bonačić-Koutecký, *J. Am. Chem. Soc.*, 2004, **126**, 2526–2535.

15 J.-H. Liu, A.-Q. Wang, Y.-S. Chi, H.-P. Lin and C.-Y. Mou, *J. Phys. Chem. B*, 2005, **109**, 40–43.
16 Z.-P. Liu, P. Hu and A. Alavi, *J. Am. Chem. Soc.*, 2002, **124**, 14770–14779.
17 T. E. Shubina, C. Hartnig and M. T. M. Koper, *Phys. Chem. Chem. Phys.*, 2004, **6**, 4215–4221.
18 J. M. Thomas, R. Raja and D. W. Lewis, *Angew. Chem., Int. Ed.*, 2005, **44**, 6456–6482.
19 B. Qiao, A. Wang, X. Yang, L. F. Allard, Z. Jiang, Y. Cui, J. Liu, J. Li and T. Zhang, *Nat. Chem.*, 2011, **3**, 634–641.
20 A. Uzun, V. Ortalan, N. D. Browning and B. C. Gates, *J. Catal.*, 2010, **269**, 318–328.
21 X.-F. Yang, A. Wang, B. Qiao, J. Li, J. Liu and T. Zhang, *Acc. Chem. Res.*, 2013, **46**, 1740–1748.
22 X. Guo, G. Fang, G. Li, H. Ma, H. Fan, L. Yu, C. Ma, X. Wu, D. Deng, M. Wei, D. Tan, R. Si, S. Zhang, J. Li, L. Sun, Z. Tang, X. Pan and X. Bao, *Science*, 2014, **344**, 616–619.
23 P. Liu, Y. Zhao, R. Qin, S. Mo, G. Chen, L. Gu, D. M. Chevrier, P. Zhang, Q. Guo, D. Zang, B. Wu, G. Fu and N. Zheng, *Science*, 2016, **352**, 797–800.
24 X. Zhang, J. Guo, P. Guan, C. Liu, H. Huang, F. Xue, X. Dong, S. J. Pennycook and M. F. Chisholm, *Nat. Commun.*, 2013, **4**, 1924.
25 G. Xu, R. Wang, F. Yang, D. Ma, Z. Yang and Z. Lu, *Carbon*, 2017, **118**, 35–42.
26 D. Deng, X. Chen, L. Yu, X. Wu, Q. Liu, Y. Liu, H. Yang, H. Tian, Y. Hu, P. Du, R. Si, J. Wang, X. Cui, H. Li, J. Xiao, T. Xu, J. Deng, F. Yang, P. N. Duchesne, P. Zhang, J. Zhou, L. Sun, J. Li, X. Pan and X. Bao, *Sci. Adv.*, 2015, **1**, e1500462.
27 H. Fei, J. Dong, M. J. Arellano-Jimenez, G. Ye, N. Dong Kim, E. L. G. Samuel, Z. Peng, Z. Zhu, F. Qin, J. Bao, M. J. Yacaman, P. M. Ajayan, D. Chen and J. M. Tour, *Nat. Commun.*, 2015, **6**, 8668.
28 Q. G. Jiang, Z. M. Ao, S. Li and Z. Wen, *RSC Adv.*, 2014, **4**, 20290–20296.
29 Y. Li, Z. Zhou, G. Yu, W. Chen and Z. Chen, *J. Phys. Chem. C*, 2010, **114**, 6250–6254.
30 P. Wu, P. Du, H. Zhang and C. Cai, *Phys. Chem. Chem. Phys.*, 2015, **17**, 1441–1449.
31 D. W. Ma, T. Li, Q. Wang, G. Yang, C. He, B. Ma and Z. Lu, *Carbon*, 2015, **95**, 756–765.
32 C. Du, H. Lin, B. Lin, Z. Ma, T. Hou, J. Tang and Y. Li, *J. Mater. Chem. A*, 2015, **3**, 23113–23119.
33 S. Lin, X. Ye, R. S. Johnson and H. Guo, *J. Phys. Chem. C*, 2013, **117**, 17319–17326.
34 X. Liu, T. Duan, Y. Sui, C. Meng and Y. Han, *RSC Adv.*, 2014, **4**, 38750–38760.
35 X. Liu, T. Duan, C. Meng and Y. Han, *RSC Adv.*, 2015, **5**, 10452–10459.
36 K. Mao, L. Li, W. Zhang, Y. Pei, X. C. Zeng, X. Wu and J. Yang, *Sci. Rep.*, 2014, **4**, 5441.
37 P. Zhao, Y. Su, Y. Zhang, S.-J. Li and G. Chen, *Chem. Phys. Lett.*, 2011, **515**, 159–162.
38 Z. Lu, P. Lv, Y. Liang, D. Ma, Y. Zhang, W. Zhang, X. Yang and Z. Yang, *Phys. Chem. Chem. Phys.*, 2016, **18**, 21865–21870.
39 C. Huang, C. Chen, X. Ye, W. Ye, J. Hu, C. Xu and X. Qiu, *J. Mater. Chem. A*, 2013, **1**, 12192–12197.
40 H. Shen, C. Duan, J. Guo, N. Zhao and J. Xu, *J. Mater. Chem. A*, 2015, **3**, 16663–16669.
41 H. Zhao, J. Song, X. Song, Z. Yan and H. Zeng, *J. Mater. Chem. A*, 2015, **3**, 6679–6684.
42 Z. Huang, X. Gu, Q. Cao, P. Hu, J. Hao, J. Li and X. Tang, *Angew. Chem.*, 2012, **124**, 4274–4279.
43 P. Hu, Z. Huang, Z. Amghouz, M. Makkee, F. Xu, F. Kapteijn, A. Dikhtiarenko, Y. Chen, X. Gu and X. Tang, *Angew. Chem., Int. Ed.*, 2014, **53**, 3418–3421.
44 B. Delley, *J. Chem. Phys.*, 1990, **92**, 508–517.
45 B. Delley, *J. Chem. Phys.*, 2000, **113**, 7756–7764.
46 J. P. Perdew, K. Burke and M. Ernzerhof, *Phys. Rev. Lett.*, 1996, **77**, 3865–3868.
47 A. Tkatchenko and M. Scheffler, *Phys. Rev. Lett.*, 2009, **102**, 073005.
48 H. J. Monkhorst and J. D. Pack, *Phys. Rev. B: Solid State*, 1976, **13**, 5188–5192.
49 T. A. Halgren and W. N. Lipscomb, *Chem. Phys. Lett.*, 1977, **49**, 225–232.
50 N. Benedek, I. Snook, K. Latham and I. Yarovsky, *J. Chem. Phys.*, 2005, **122**, 144102.
51 Y. Inada and H. Orita, *J. Comput. Chem.*, 2008, **29**, 225–232.
52 J. H. Kwak, J. Hu, D. Mei, C.-W. Yi, D. H. Kim, C. H. F. Peden, L. F. Allard and J. Szanyi, *Science*, 2009, **325**, 1670–1673.
53 S. Sun, G. Zhang, N. Gauquelin, N. Chen, J. Zhou, S. Yang, W. Chen, X. Meng, D. Geng, M. N. Banis, R. Li, S. Ye, S. Knights, G. A. Botton, T.-K. Sham and X. Sun, *Sci. Rep.*, 2013, **3**, 1775.
54 M. D. Esrafili, N. Saeidi and P. Nematollahi, *RSC Adv.*, 2015, **5**, 100290.
55 C. Jin, F. Lin, K. Suenaga and S. Iijima, *Phys. Rev. Lett.*, 2009, **102**, 195505.
56 Z. Lu, P. Lv, J. Xue, H. Wang, Y. Wang, Y. Huang, C. He, D. Ma and Z. Yang, *RSC Adv.*, 2015, **5**, 84381–84388.
57 E. H. Song, Z. Wen and Q. Jiang, *J. Phys. Chem. C*, 2011, **115**, 3678–3683.
58 S. Lin, X. Ye and J. Huang, *Phys. Chem. Chem. Phys.*, 2015, **17**, 888–895.
59 M. D. Esrafili and N. Saeidi, *Struct. Chem.*, 2015, **27**, 595–604.
60 S. Chakrabarty, T. Das, P. Banerjee, R. Thapa and G. P. Das, *Appl. Surf. Sci.*, 2017, **418**(Part A), 92–98.
61 D. Tang and C. Hu, *J. Phys. Chem. Lett.*, 2011, **2**, 2972–2977.
62 O. Leenaerts, B. Partoens and F. M. Peeters, *Phys. Rev. B: Condens. Matter Mater. Phys.*, 2008, **77**, 125416.
63 S. Abdel Aal, *Surf. Sci.*, 2016, **644**, 1–12.
64 E. W. Kuipers, A. Vardi, A. Danon and A. Amirav, *Phys. Rev. Lett.*, 1991, **66**, 116–119.
65 F. Li, J. Zhao and Z. Chen, *J. Phys. Chem. C*, 2012, **116**, 2507–2514.
66 S. Sinthika, S. T. Vala, Y. Kawazoe and R. Thapa, *ACS Appl. Mater. Interfaces*, 2016, **8**, 5290–5299.
67 I. H. Lin, Y.-H. Lu and H.-T. Chen, *Phys. Chem. Chem. Phys.*, 2016, **18**, 12093–12100.
68 Z. Lu, S. Li, D. Ma, Y. Zhang, X. Yang, C. He, X. Wang and Z. Yang, *J. Mater. Sci.*, 2016, **51**, 10400–10407.

69 Z. Lu, D. Ma, L. Yang, X. Wang, G. Xu and Z. Yang, *Phys. Chem. Chem. Phys.*, 2014, **16**, 12488–12494.
70 C. Liu, Y. Tan, S. Lin, H. Li, X. Wu, L. Li, Y. Pei and X. C. Zeng, *J. Am. Chem. Soc.*, 2013, **135**, 2583–2595.
71 D. Tang, Z. Chen, J. Hu, G. Sun, S. Lu and C. Hu, *Phys. Chem. Chem. Phys.*, 2012, **14**, 12829–12837.
72 Y.-H. Lu, M. Zhou, C. Zhang and Y.-P. Feng, *J. Phys. Chem. C*, 2009, **113**, 20156–20160.
73 Y. Tang, Z. Yang and X. Dai, *Phys. Chem. Chem. Phys.*, 2012, **14**, 16566–16572.
74 M. D. Esrafili and N. Saeidi, *Phys. E*, 2015, **74**, 382–387.
75 Y. Tang, W. Chen, Z. Shen, S. Chang, M. Zhao and X. Dai, *Carbon*, 2017, **111**, 448–458.
76 C. Huang, X. Ye, C. Chen, S. Lin and D. Xie, *Comput. Theor. Chem.*, 2013, **1011**, 5–10.
77 S. Sinthika, E. M. Kumar and R. Thapa, *J. Mater. Chem. A*, 2014, **2**, 12812–12820.
78 Z. Lu, S. Li, P. Lv, C. He, D. Ma and Z. Yang, *Appl. Surf. Sci.*, 2016, **360**(Part A), 1–7.
79 R. R. Chianelli, G. Berhault, P. Raybaud, S. Kasztelan, J. Hafner and H. Toulhoat, *Appl. Catal., A*, 2002, **227**, 83–96.
80 T. Jiang, D. J. Mowbray, S. Dobrin, H. Falsig, B. Hvolbæk, T. Bligaard and J. K. Nørskov, *J. Phys. Chem. C*, 2009, **113**, 10548–10553.
81 D. Yuan, Z. Han, G. Czap, C.-l. Chiang, C. Xu, W. Ho and R. Wu, *J. Phys. Chem. Lett.*, 2016, **7**, 2228–2233.
82 P. Zhang, X. F. Chen, J. S. Lian and Q. Jiang, *J. Phys. Chem. C*, 2012, **116**, 17572–17579.
83 Y. Li and Q. Sun, *Sci. Rep.*, 2014, **4**, 4098.
84 M. D. Esrafili, R. Mohammad-Valipour, S. M. Mousavi-Khoshdel and P. Nematollahi, *ChemPhysChem*, 2015, **16**, 3719–3727.
85 D.-H. Lim and J. Wilcox, *J. Phys. Chem. C*, 2012, **116**, 3653–3660.